Wind Tunnel Testing of AFC over a Deflected Aileron on the High-Lift Common Research Model

LaTunia Pack Melton*, Mehti Koklu†, Marlyn Y. Andino‡, and Judith A. Hannon§
NASA Langley Research Center, Hampton, Virginia, United States of America

Active flow control (AFC) using discrete fluidic actuators distributed along the span, just upstream of the deflected aileron of the 10% scale high-lift version of the Common Research Model (CRM-HL), was evaluated during a wind tunnel test in the NASA Langley 14- by 22-Foot Subsonic Tunnel. For this set of experiments, a new outboard section was fabricated incorporating a deflectable aileron. Aileron deflection angles of 0°, 7.5°, 16°, and 25° were investigated. This experimental investigation is in response to a recent study by Boeing indicating the potential to use AFC with a drooped aileron during takeoff to improve lift-to-drag ratio (L/D) by as much as 5%, depending on AFC mass flow rate. AFC is used at deflection angles above the nominal deflection of 7.5° to control the resulting flow separation that occurs and potentially improve L/D. Improvements in aircraft low-speed L/D can affect vehicle range and/or payload. Tuft flow visualization data, steady and unsteady surface pressure data, and force and moment data are used to compare the flowfields with and without AFC. Parameters varied include actuator momentum coefficient and aileron deflection angle. The surface pressure and tuft flow visualization results indicate that without AFC, the flow over a majority of the aileron upper surface is separated for aileron deflection angles larger than 7.5°. When AFC is applied, the flow is reattached to the aileron. Force and moment results show that a local increase in lift leads to an increase in L/D of at least 3.5% using mass flow rates thought to be available from air sources onboard a commercial transport.

Nomenclature

Ail	aileron deflection angle, degrees
C_D	drag coefficient
b	wing semispan
c	mean aerodynamic chord, 27.58 inches at y = 46.875 inches
C_L	lift coefficient
c_L	sectional lift coefficient
C_p	pressure coefficient, $(P - P_\infty)/q_\infty$
$C_{p,TE}$	trailing edge C_p
C_q	mass flow coefficient, $\dot{m}/(\rho U_\infty S_{ref})$
h	height of actuator nozzle
L/D	lift-to-drag ratio lift/drag
M	Mach number
$\dot{m}$	mass flow rate, $\rho U_{jet} A_{jet} n_{jet}$
NPR	nozzle pressure ratio, P_s/P_∞
P	pressure
P_∞	freestream static pressure
P_s	actuator inlet static pressure
q_∞	freestream dynamic pressure, $1/2\rho_\infty U_\infty^2$
Re_c	Reynolds number based on mean aerodynamic chord (c)
S_{ref}	reference surface area
U_{jet}	actuator nozzle velocity

*Research Scientist, Flow Physics and Control Branch, MS 170, Associate Fellow AIAA.
†Research Scientist, Flow Physics and Control Branch, MS 170, Member AIAA.
‡Research Scientist, Flow Physics and Control Branch, MS 170, Senior Member AIAA.
§Research Scientist, Flow Physics and Control Branch, MS 170

U_∞	freestream velocity
w	width of actuator nozzle
x, y, z	model coordinate system
α	angle of attack, deg
δ_f	flap deflection angle, degrees
δ_s	slat deflection angle, degrees
η	normalized semispan, y/b
Λ	sweep angle, deg
ρ_∞	freestream air density

Abbreviations

14x22	14- by 22-Foot Subsonic Tunnel
3D	three dimensional
AFC	active flow control
Ail	aileron
AATT	Advanced Air Transport Technology
CD	convergent-divergent nozzle
CHL	conventional high lift
CRM-HL	High-Lift version of the Common Research Model
CRM-SHL-AFC	Simplified High-Lift version of the Common Research model
LaRC	Langley Research Center
lb	pounds
nm	nautical miles
psf	pounds per square foot
SLA	stereolithography
STJ	steady jet
SWJ	sweeping jet
SHL	simplified high lift
sp	spacing
unc	uncorrected
VSTOL	vertical short takeoff and landing

I. Introduction

Active flow control (AFC) had been demonstrated to be effective in improving the aerodynamic efficiency of high-lift systems on commercial transports. For this reason, it has been a technology investment area for the NASA Advanced Air Transport Technology (AATT) Project. AATT focuses on advancing technologies that may improve the energy efficiency and environmental compatibility of future commercial transports. AFC is considered one of the technologies that may contribute to reaching net zero greenhouse gas emissions by 2050. However, a challenge often faced by promising AFC applications is the impact or cost of the technology when integrated into an aircraft. The current experimental campaign leverages the 10% scale high-lift version of the Common Research (CRM-HL), a relevant high-lift configuration originally built for AFC testing, and the lessons learned from that AFC research. Additionally, the initial AFC research on the CRM-HL model was a joint NASA/Boeing effort and discussions about opportunities for future applications and research needs helped to lay the groundwork for the current research effort.

The 10% scale CRM-HL semispan model was designed as a test article to assess the viability of various active flow control (AFC) approaches. Testing of the 10% scale CRM-HL model with active flow control (AFC) on the aileron followed the successful wind tunnel test campaign where AFC was applied upstream of the flap of the CRM-HL model equipped with a simple-hinged flap (CRM-SHL-AFC) [1, 2]. In the first AFC test using the 10% scale CRM-HL [2, 3], simple-hinged inboard and outboard flaps with various types of pneumatic actuators near the flap hinge line were evaluated to determine the aerodynamic feasibility of replacing the Fowler flaps. Replacing the conventional Fowler flaps with simple-hinged flaps augmented by AFC was shown by Hartwich et al. [4] to reduce fuel burn by up

to 2.25%. This reduction in fuel burn was attributed primarily to eliminating the flap track fairings associated with the Fowler flaps. Results of the CRM-SHL-AFC test campaign indicated that simple-hinged flaps could be used to match the lift performance of a conventional high-lift configuration with slotted Fowler flaps. Several candidate actuator configurations were tested in an attempt to achieve the targeted lift performance. The large adverse pressure gradient present on the CRM-SHL-AFC with 50° inboard and 55° outboard flaps required the use of an actuation concept called the High Efficiency Low Power (HELP) actuator [1, 2]. Although the actuation in conjunction with the flap configuration was successful in recovering the lift, the changes to the wing geometry and the significant amount of AFC momentum required to control separation made the CRM-SHL-AFC configuration a far-term technology for improving fuel burn on a commercial transport.

Following the AFC studies using the CRM-SHL-AFC, our AFC research pivoted to possible localized applications of AFC that could be integrated into an existing aircraft design and powered by onboard air sources. Shmilovich et al. [5–7] explored several localized applications of active flow control capable of improving L/D, lift (L) and/or reducing drag (D) at takeoff and/or landing conditions. Based on the results of these studies, the application of AFC to the aileron was selected to implement on the 10% scale CRM-HL model in the NASA Langley 14- by 22-Foot Subsonic Tunnel (14x22). During takeoff, the ailerons are typically deflected symmetrically to a nominal deflection angle of 7.5°. Computational Fluid Dynamic (CFD) simulations indicated that applying AFC to the aileron during takeoff could potentially improve L/D by as much as 5%. A 1% improvement in L/D has been estimated by Garner et al. [8] to be equivalent to a 2,800 lb increase in payload or a 150 nm increase in range for a large, generic twin engine transport aircraft. These potential improvements in the efficiency of a commercial transport motivated the AFC aileron experimental wind tunnel test campaign.

The application of AFC on the "drooped" aileron is similar to the AFC research on the "drooped' flap of the CRM-SHL-AFC configuration in that momentum is introduced into the flowfield upstream of the natural separation point in an attempt to reduce flow separation. Several studies have shown that this approach is successful in reducing or eliminating flow separation thereby increasing lift. Unlike the CRM-SHL-AFC configuration, the aileron deflection angles are much smaller. These small deflection angles, when compared to the SHL deflection angles, result in separated flowfields that require less momentum input to control. Shmilovich et al [5, 6] examined several types of actuation ranging from steady blowing through a continuous spanwise slot to discrete ducts on the aileron of a computational reference aircraft (CRA). The CRA used for the study is representative of a conceptual future short/medium range, twin-engine transonic airplane. A system integration study by Vijgen et al. [9, 10] took the CRA results and translated them onto a performance reference configuration to determine the benefit after the AFC system was integrated into the vehicle. They explored the use of auxiliary power unit (APU), engine bleed, and auxiliary compressors as options for the pneumatic sources required for the AFC system. They concluded with a ranking of each option where availability, practicality, and weight are considered. Supplying air to the AFC aileron system using the existing compressor (with engine bleed backup) was an option that received a high rating in terms of overall practicality.

The goal of our experimental study was to determine the increment in L/D that can be achieved when applying AFC to the aileron of the 10% scale CRM-HL model. After a description of the test facility, model geometry, and installation, we begin the results section with a discussion of data repeatability. The repeatability section is included because of the small increments in lift and decrements in drag when applying AFC on the aileron. Next, results are presented comparing the aerodynamic performance of the AFC-off CRM-HL model with Ail=7.5°, 16°, and 25°. Then, results for the application of AFC at the two higher aileron deflections angles are presented and discussed. Finally, we present some preliminary L/D results. Surface static pressure measurement, balance force and moment results, and mini tuft flow visualization results are used to assess the benefit of the AFC aileron on the CRM-HL model. Due to the test being recently completed, absolute quantities for L/D are not included in this report. However, increments are used to show the effect of the AFC aileron.

II. Experiment and Model Description

The experiment was conducted in the NASA Langley Research Center (LaRC) 14x22. The 14x22 is a closed-circuit wind tunnel with a 9:1 contraction ratio that was built for VSTOL testing in 1970. The test section has multiple configuration options that include closed, slotted, partially open and open [11]. Reference [11] provides an overview of the facility capabilities that include a boundary layer removal system and optical access for measurement techniques such as Particle Image Velocimetry (PIV), Laser Doppler Velocimetry, and photogrammetry. The boundary layer removal system was not used during the test. For the current CRM-HL AFC experiment, we tested with the closed configuration. In this tunnel configuration, the test section is 14.5 ft high by 21.75 ft wide by 50 ft long and the maximum speed is

338 ft/sec. The tunnel test section consists of two streamwise bays into which various facility model support carts are installed. Semispan models like the CRM-HL are floor-mounted on a cart in the forward part of the test section [11]. The turbulence intensity in the tunnel is between 0.07 and 0.08 percent at a dynamic pressure (q_∞) of 60 psf; however, it varies with q_∞ and with location [12]. All quantitative data presented were acquired at a Mach number of $M = 0.2$ ($q_\infty \approx 60$ psf) resulting in a Reynolds number based on the mean aerodynamic chord (Re_c) of approximately 3.0×10^6 . Temperature is not controlled in the 14x22 so with M fixed, the Re_c varies slightly because of temperature variations. Facility data can be corrected using classical correction methods, the Heyson method [13], and the Transonic Wall Interference Correction System (TWICS), which is based on a wall signature method. Data are currently being reduced using the TWICS method. Wall corrected data from the CRM-SHL-AFC tests of the model in the 14x22 were corrected using the TWICS correction method[1, 2].

A. CRM-HL

Originally built for aeroacoustic and active flow control testing [1, 2, 14], the 10% scale semispan CRM-HL model (Fig. 1), with a new outboard wing section, was tested in the reference takeoff configuration defined by Lacy and Clark [15]. Table 1 summarizes the model dimensions. In the takeoff configuration, the leading edge slat deflection is 22° and the trailing edge flap deflections are 25° for both the inboard and outboard flaps. Additionally, the leading edge slat is sealed [15]. Fifteen slat brackets, three for the inboard slat and 12 for the outboard slat, were manufactured using direct metal laser sintering to secure the slat to the wing under slat surface (WUSS). The slat brackets were designed with channels for routing pressure tubing to the WUSS, eliminating the need to route tubing bundles external to the brackets. Two brackets, one internal and one external, connect the inboard flap to the main element and two external brackets support the outboard flap. These brackets are covered by polycarbonate flap fairings that also cover the outboard flap pressure tubing that is routed through the main wing. The model is mounted on top of a 3.5 inch peniche and includes a strake at the junction between the fuselage and wing leading edge. Similar to the landing configuration [16], the nominal takeoff configuration includes a nacelle chine. The nacelle has the original inlet lip and does not have the modification referred to in Ref. [15]. Transition dots with a height of 0.254 mm (0.01 inches) and a diameter of 1.27 mm (0.05 inches) were installed on the model following the trip dot installation description available for the fourth High-Lift Prediction Workshop [17] that used the result of Lacy and Clark [15] and Evans et al. [18]. Figure 2 shows the pressure orifice layout of the 10% scale CRM-HL model in the takeoff configuration with the AFC aileron installed. Compared to the original outboard section, there are fewer pressure orifices due to the addition of the AFC air supply lines that will be discussed in the next section. Streamwise pressures at $\eta = 82\%$ and $\eta = 91\%$ are labeled in Fig. 2 since these two locations are affected most by aileron AFC.

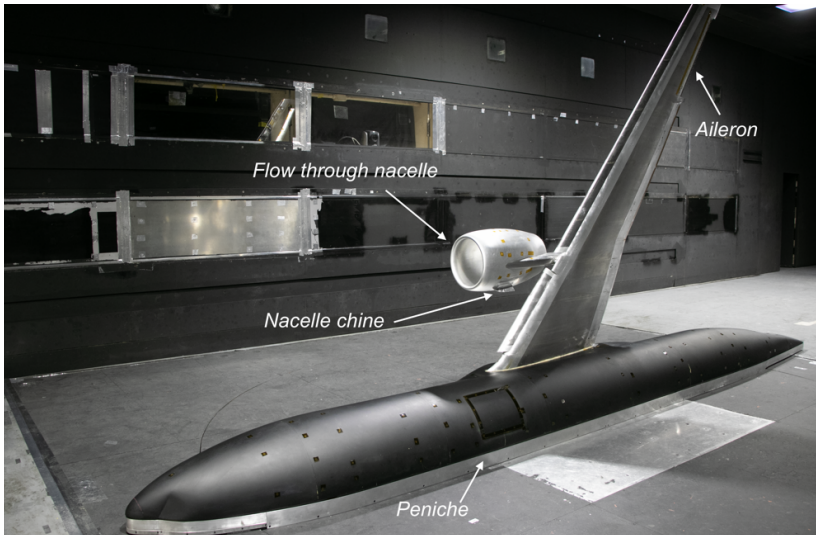

Fig. 1 CRM-HL model in the 14x22 [Source: NASA].

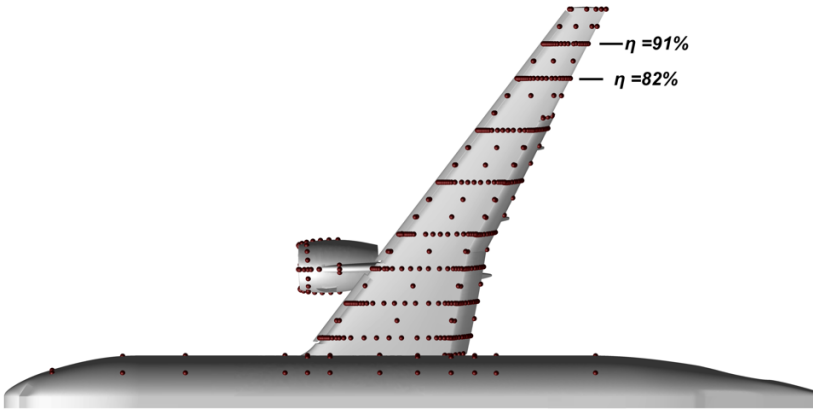

Fig. 2 CAD model with pressure orifices denoted by dots.

Table 1 10% scale CRM-HL model geometry information.

Parameter	Symbol	Value	
		SI	English
Mean aerodynamic chord	c	701 mm	27.6 in
Wing Semispan	b	2938 mm	115.7 in
Reference area of semispan wing	S_{ref}	1.918 m^2	2973.6 in^2
Sweep angle at wing quarter chord	Λ	35°	
Aspect Ratio	AR	9	

B. AFC-Aileron

The 10% scale CRM-HL model was designed to be modular to accommodate options such as a future aileron design (Fig. 3(a)). At the junction between the inboard (just outboard of the outboard flap) and the outboard wing sections, a 25.4 mm (1 inch) diameter hole/passage way was included to route instrumentation and AFC air lines for flow control. Boeing defined an aileron for the CRM-HL planform [6], and the wind tunnel hardware was designed at LaRC. The new outboard wing section of the CRM-HL was designed to include an aileron with fixed brackets for aileron deflection angles of 0°, 7.5°, 16°, and 25°. CFD simulations indicated a potential benefit in L/D by using AFC to control separation on ailerons deflected beyond the nominal deflection angle of 7.5° [5, 6]. Similar to the CRM-SHL-AFC model design [1, 2], the aileron design included a region where AFC actuator cartridges, manufactured using stereolithography, could be installed. Using lessons learned from the 2018 CRM-SHL-AFC test, the cartridges did not include pressure or thermocouple instrumentation. This instrumentation was included in other regions of the wing that were fixed throughout the test. The red arrows shown in Fig. 3(b) indicate the fixed locations where the pressures, P_s, used to compute NPR for each actuator cartridge were measured. Thermocouples were installed in the supply lines closer to the valves used to control mass flow rate. Both sweeping jet actuators (SWJ) and convergent-divergent (CD) steady jet actuators (STJ) were manufactured and tested. Parameters investigated included actuator spacing, mass flow rate, and NPR. The design of the AFC cartridge installation for the aileron allowed multiple passive and active flow control actuator configurations to be evaluated. Three actuator cartridges (Fig. 3(a)), covering the span of the aileron, were used for AFC. The mass flow rate to each cartridge could be independently controlled. Figure 3(b) shows the internal routing of the plumbing used for control. Each actuator cartridge has two air input ports. Actuator inlet static pressure, P_s, was measured in each input port and the average used to compute NPR for each cartridge. Due to the smaller adverse pressure gradient generated by deflecting the aileron when compared to CRM-SHL-AFC configuration [1, 2], the mass flow requirements were significantly reduced. An upstream Venturi flowmeter was used to measure total mass flow rate. Additionally, three thermal mass flow meters installed downstream of the control valves for the three

AFC actuator cartridges were used to measure the mass flow rate supplied to each AFC cartridge. The AFC air supply system was relocated relative to the layout tested in Ref. [19]. Additionally, the hoses used for the AFC air delivery system were flexible and were routed through the center of the balance to minimize hose and tare interference. The 2-inch diameter high volume shop air line, used for facility model cart moves, served as the supply air source for the aileron actuator cartridges.

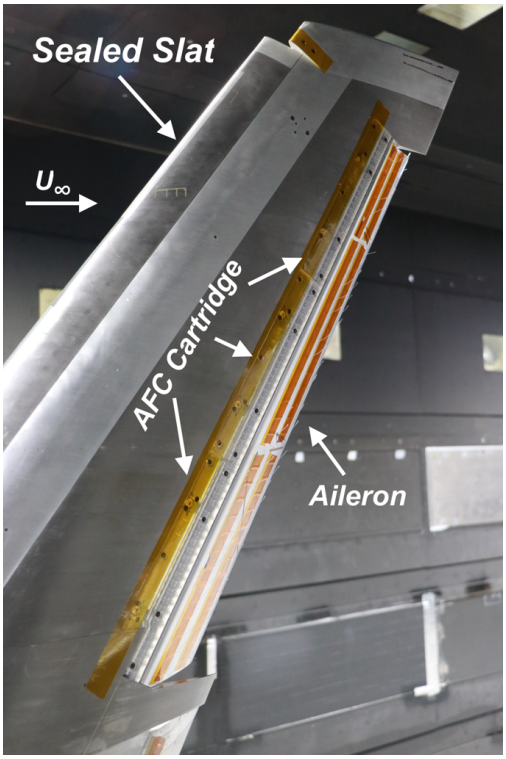

(a) Close-up, top view of aileron [Source: NASA].

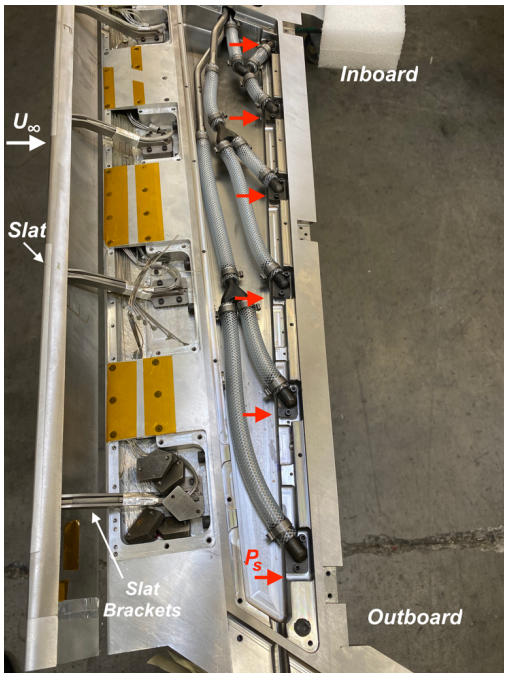

(b) Internal cavity view of outboard wing lower surface (aileron and lower surface hatch cover not installed). Red arrows denote P_s measurement locations [Source: NASA].

Fig. 3 Images of CRM-HL model outboard wing section with AFC-enhanced aileron.

Both the SWJ and STJ actuators used for the investigation had width to height ratios at the exit of 2:1 and all actuator orifice dimensions (1.12 mm w x 0.55 mm h) were identical. The actuator height was limited by the outer mold line (OML) of the CRM-HL model at the trailing edge of the main element. With this limit on actuator height, the width was selected based on the study of Koklu [20] who found 2:1 to be the optimal aspect ratio for a sweeping jet. Shmilovich et al. [6] also recommended this aspect ratio for the aileron AFC actuators on the CRM-HL model. Spacing of SWJ and STJ actuators was varied with spacings (sp) 1, 2, and 3, corresponding to 69, 35, and 18 actuators, respectively. Table 2 summarizes the actuator configurations that were evaluated. Results for SWJ1, SWJ2, and SWJ3 actuators are presented in this paper.

III. Results

In this section, we present selected initial results from the wind tunnel test campaign focused on applying AFC to the drooped aileron of the 10% scale CRM-HL model in the 14x22. We begin by examining the performance characteristics as the aileron deflection is varied with AFC off. Following this, we present results with AFC applied and discuss the impact of AFC on the performance and flow field with the drooped aileron. Unless otherwise specified, the results presented use data that has not been corrected for wind tunnel wall interference.

Table 2 Aileron actuator cartridge configurations.

Actuator Designation	Actuator Type	Inboard Quantity	Midboard Quantity	Outboard Quantity	Total nozzle area, mm^2
SWJ1	SWJ	23	23	23	43.1
SWJ2	SWJ	12	11	12	21.9
SWJ3	SWJ	6	6	6	11.2
CD1	STJ	23	23	23	43.1
CD2	STJ	12	11	12	21.9

A. Data Repeatability AFC Off

Prior to presenting and discussing the results of the aileron AFC study, selected data repeatability information is provided. These repeatability results aid in understanding our confidence in the data being presented, including the increments in L/D. The approach taken by Wahls et al. [21] to understand the data repeatability results from the National Transonic Facility and by Hannon et al. [22] when assessing the repeatability of data from the Trapezoidal Wing configuration tested in 14x22 was used. In this approach, we curve fit the data using a least squares polynomial and then use the residuals for each data point from the curve fit to calculate prediction intervals (95% confidence level). Prediction intervals are bounds that if another data point is acquired there is a 95% chance it will fall within these bounds. This analysis was done for aileron deflections of 7.5°, 16°, and 25° over an α range of 0° to 10°, i.e., results are in the linear range of the C_L vs α curve and cover the α region of primary interest for determining the L/D increment due to AFC.

Table 3 shows the prediction intervals for C_L, C_D, and L/D for the three aileron deflections. Figure 4 shows the L/D residuals and prediction intervals (red dashed line) for the aileron deflections. The numbers in the legend denote the corresponding test point at which the data was obtained. Also shown in Fig. 4 is the expected instrumentation uncertainty confidence level (blue dashed line). These levels are also based on 95% and were calculated using propagation of errors through the data reduction equations. The L/D variation during the test was within the instrumentation uncertainty for the three aileron deflections without any active flow control.

Table 3 Prediction interval, AFC off.

Ail	C_L	C_D	L/D
7.5°	± 0.0048	± 0.0005	± 0.0861
16°	± 0.0091	± 0.0008	± 0.1466
25°	± 0.0053	± 0.0006	± 0.0744

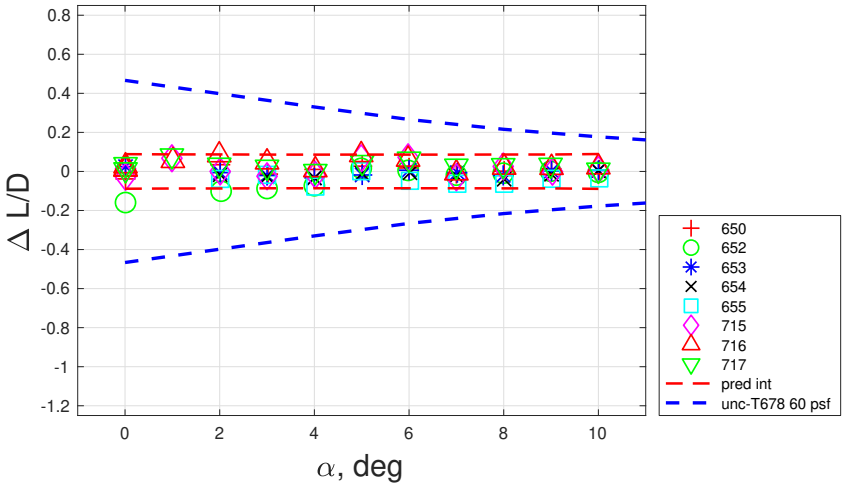

(a) $Ail = 7.5°$.

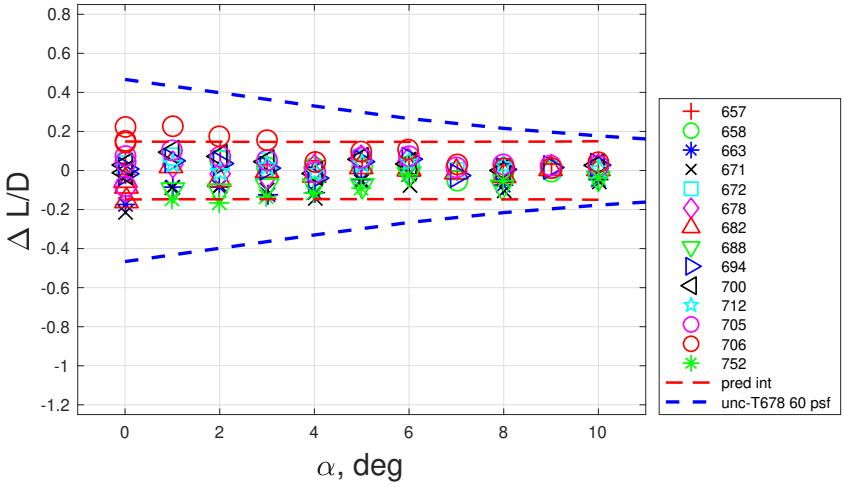

(b) $Ail = 16°$.

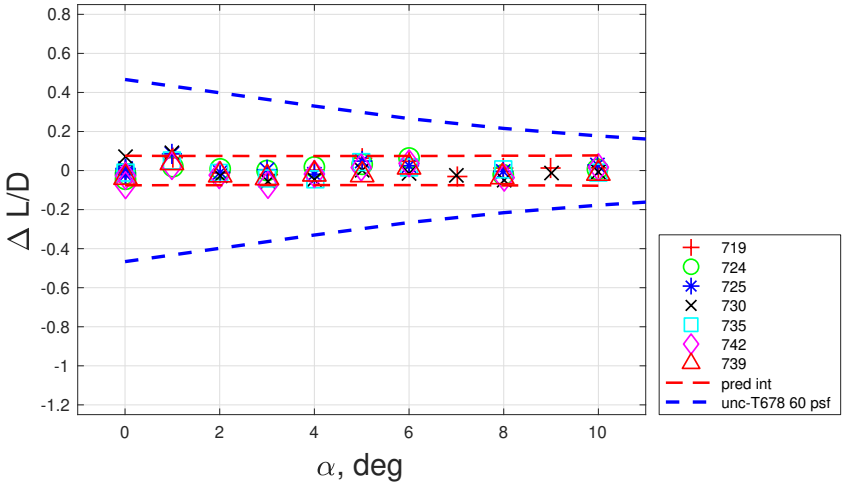

(c) $Ail = 25°$.

Fig. 4 L/D residuals ($M = 0.2$, $Re_c = 3.0x10^6$, $q_\infty = 60$ psf).

B. CRM-HL Takeoff Characteristics, Aileron AFC Off

During takeoff, a 7.5° symmetric deflection of the ailerons is typically used to increase L/D. Figure 5 shows the aerodynamic performance of the CRM-HL model as the aileron deflection angle is increased. C_L values relative to the lift value at $Ail = 7.5°$ are presented in Fig. 5(a) for three angles of attack ($\alpha = 4°, 6°$, and $8°$), all in the linear region of C_L vs. α. As the aileron is deflected, wing camber is increased causing $C_L/C_{L,7.5}$ to increase (Fig. 5(a)). A byproduct of the larger aileron deflection angles is the generation of a larger adverse pressure gradient accompanied by aileron flow separation. Therefore, the increment in C_L is accompanied by an increase in C_D (Fig. 5(b)) caused by the larger form drag at Ail =16° and 25°, indicating circulation increases in this span region due to the increased camber with the deflected aileron. For $Ail > 7.5°$, L/D is reduced when compared to the nominal Ail of 7.5° (Fig. 5(c)). Shmilovich et al. [5] show similar trends thus explaining why $Ail = 7.5°$ is the nominal takeoff aileron setting.

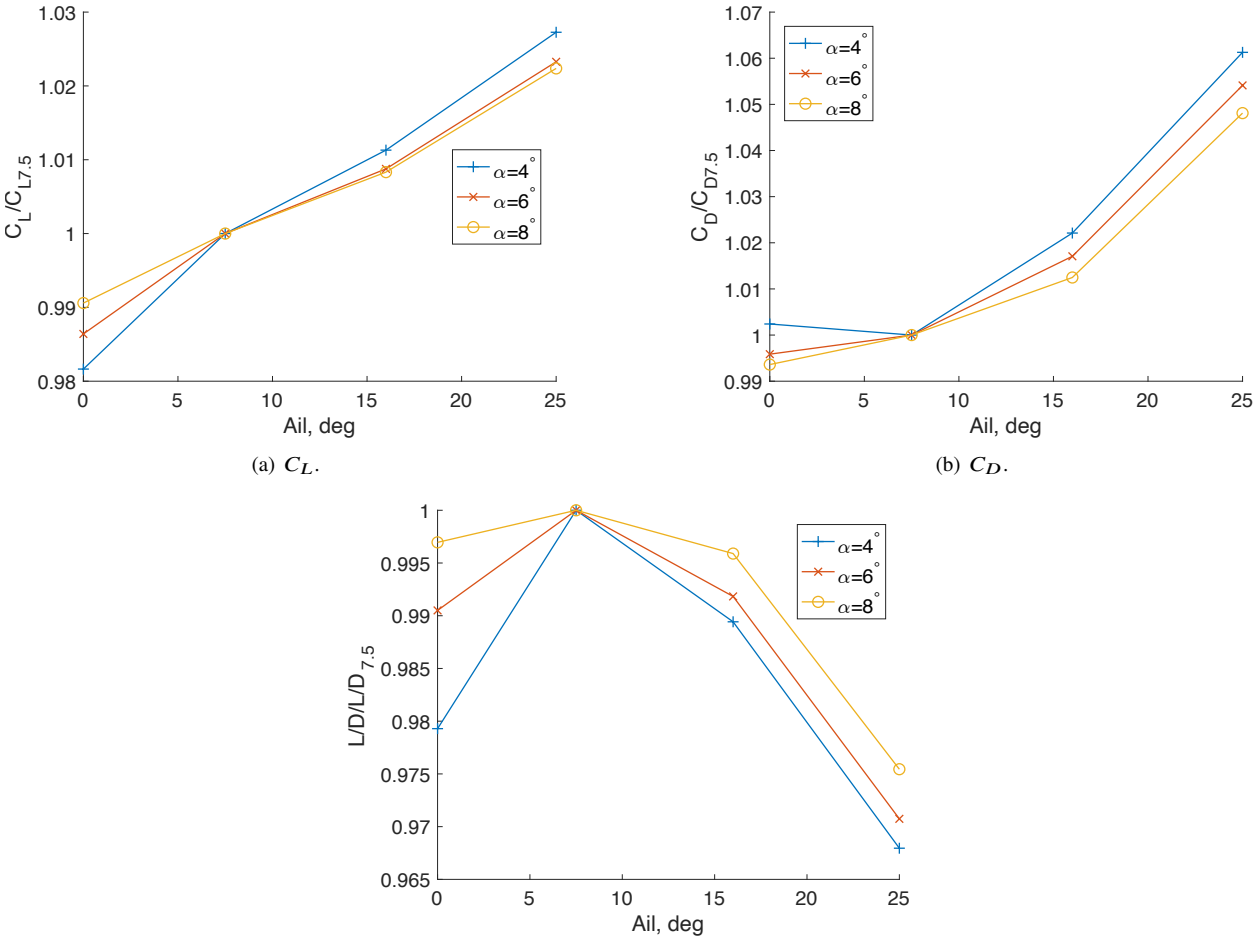

(a) C_L.

(b) C_D.

(c) L/D.

Fig. 5 Effect of aileron deflection (AFC-off) on C_L, C_D, and L/D ($M = 0.2$, $Re_c = 3.0x10^6$, $q_\infty = 60$ psf).

To determine the local changes to the flowfield on the outboard section of the wing, we examine the pressure distributions at the two streamwise location ($\eta = 0.82$ and $\eta = 0.91$) on the aileron labeled in Fig. 2). C_p distributions at $\alpha = 4°$ are presented in Fig. 6 that illustrate varying levels of flow separation on the aileron as Ail increases. An increase in circulation at $\eta = 82\%$ and $\eta = 91\%$ is evident by the increase in suction pressure over the entire section, including the slat. The plateaus in C_p for $x > 174$ shown in Fig. 6(a) at $\eta = 82\%$ and for $x > 180$ in Fig. 6(b) at $\eta = 91\%$ indicate that the flow on the aileron is separated for Ail=16° and 25°. At these two spanwise locations the flow appears to separate at the aileron leading edge. Lower pressures are observed not only on the aileron but for the entire upper surface as the aileron deflection angle increases, indicating circulation increases in this specific region due to the increased camber with the deflected aileron. For $Ail = 0°$, there is pressure recovery at the trailing edge indicating

attached flow over the majority of the aileron at both locations. A small region of separated flow is present near the trailing edge of the aileron at $Ail = 7.5°$, as evidenced by the slight deviation in the slope of C_p vs. x when compared to the $Ail = 0°$ results. Unlike the larger aileron deflections ($Ail = 16°$ and $Ail = 25°$) this small amount of separation has a smaller effect on C_D as shown in Fig. 5(b).

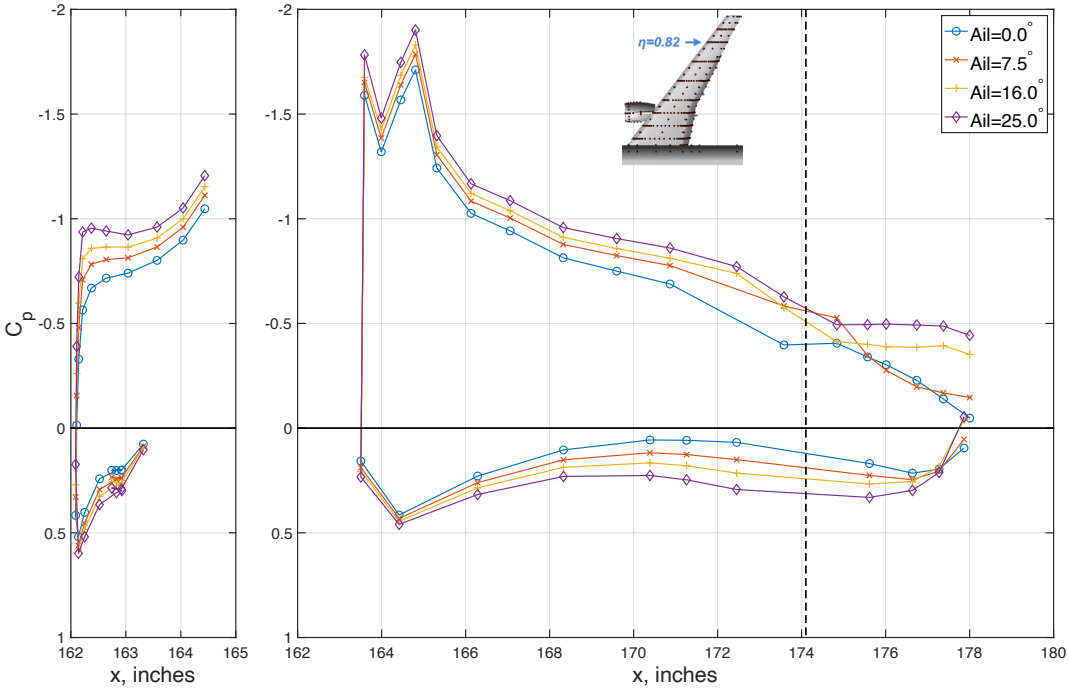

(a) $\eta = 82\%$.

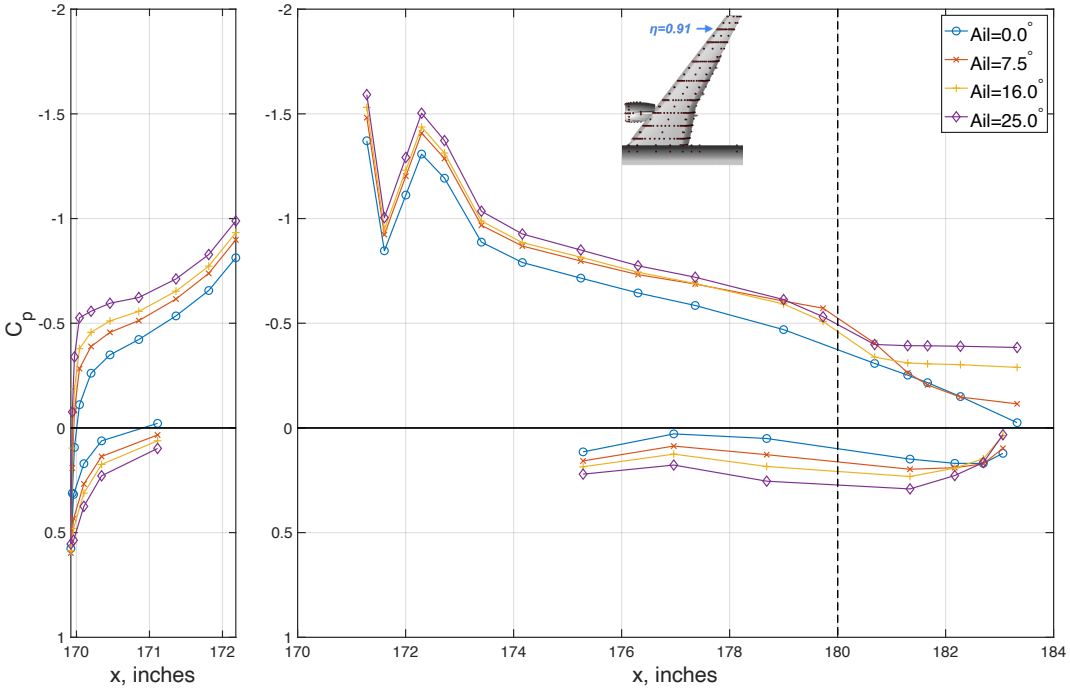

(b) $\eta = 91\%$.

Fig. 6 Effect of aileron deflection (AFC-off) on C_p at two outboard wing stations ($M = 0.2$, $Re_c = 3.0x10^6$, $q_\infty = 60$ psf). Vertical dashed line represents junction between main wing and aileron.

One of the six unsteady pressure sensors on the aileron was used to compare the flowfields for Ail values of 0°, 7.5°, 16°, and 25°. The sensor selected for the comparison is located just inboard of the most upstream aileron static pressure orifice at $\eta = 0.82$ as shown in the inset image in Fig. 7. A row of unsteady pressures was included upstream on the aileron to provide information on SWJ actuator oscillation frequency. Downstream sensors, near the aileron trailing edge, were included to provide information about flow unsteadiness due to varying levels of separated flow. Pressure spectra from the sensor near $\eta = 0.82$ is shown in Fig. 7. Like the mean C_p values in Fig. 6, the spectra show that the pressure fluctuations at this location for $Ail = 0°$ and 7.5° are similar. For higher Ail values (16° and 25°), there is a notable rise in the low frequency pressure fluctuations and a reduction in pressure fluctuations for frequencies above 2 Khz – 3 Khz. Increases in low frequency pressure oscillations are associated with the low frequency oscillations of the separated shear layer above the aileron at this location. Another indicator of separated flow at this sensor location for $Ail = 16°$ and 25° is the reduction in pressure fluctuations at the higher frequencies.

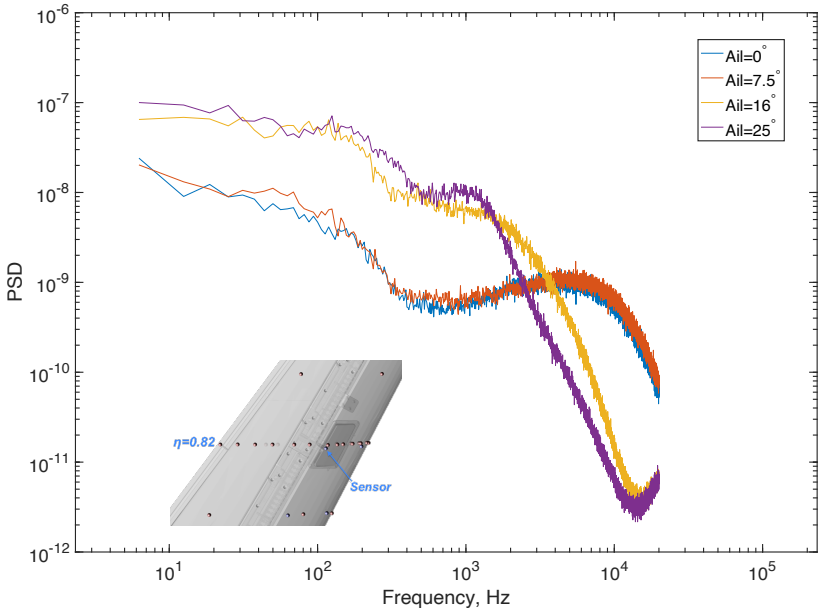

Fig. 7 Effect of aileron angle on unsteady pressure spectra (AFC-off) ($Re_c = 3.0x10^6$, $M = 0.2$, $q_\infty = 60$ psf, $\alpha = 4°$).

Mini tuft flow visualization images are presented in Figs. 8 to help illustrate the varying levels of separated flow present on the aileron as the deflection angle is increased (AFC-off) for $\alpha = 4°$. The tuft images complement the C_p results by providing details about the flowfield over the entire aileron. The undeflected ($Ail = 0°$) aileron has attached flow, causing the tufts to be in the streamwise direction (Fig. 8(a)). It should be noted that although results for this aileron deflection angle are at $M = 0.15$, the results are identical to those obtained at $M = 0.2$. When the aileron deflection angle is increased to $Ail = 7.5°$, unsteady flow is evident by the blurred 'fan-like' tuft patterns. The tufts near the trailing edge of the aileron are directed toward the wing tip, a sign that the spanwise component of velocity is larger than the streamwise component. The spanwise flow at the trailing edge of the aileron at $Ail = 7.5°$ is in agreement with the small region of separated flow observed in the C_p distribution (Fig. 6). Three-dimensional (3D) flow separation causes the tufts to be directed upstream and toward the wing tip at $Ail = 16°$ and $Ail = 25°$ (Fig. 8(c) – Fig. 8(d)). Additionally, the fan-like tuft pattern is an indicator of flow unsteadiness. Some features that differentiate $Ail = 16°$ from $Ail = 25°$ is that there is an upstream, inboard region of attached flow, evidenced by the streamwise tufts at $Ail = 16°$ presented in Fig. 8(c). And, at $Ail = 25°$ (Fig. 8(d)), along the inboard edge of the aileron, the tufts point inboard. This may be due to a vortex that is formed at the inboard aileron edge causing the most inboard tufts to point toward the undeflected fixed trailing edge between the aileron and the deflected outboard flap, while the adjacent row of tufts are directed toward the wing tip.

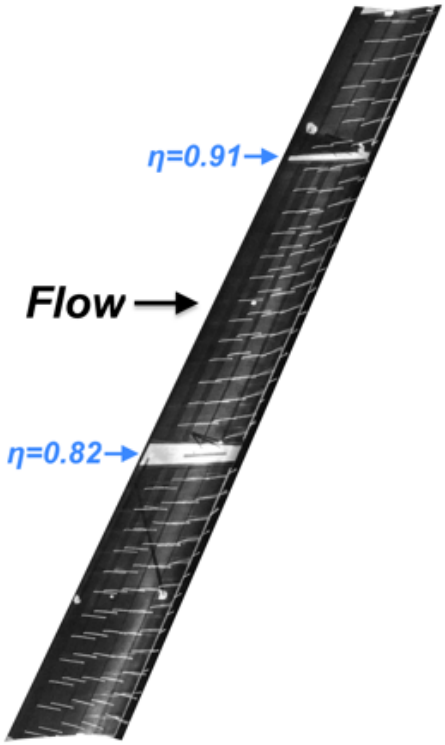

(a) $Ail = 0°, M = 0.15$.

(b) $Ail = 7.5°, M = 0.20$.

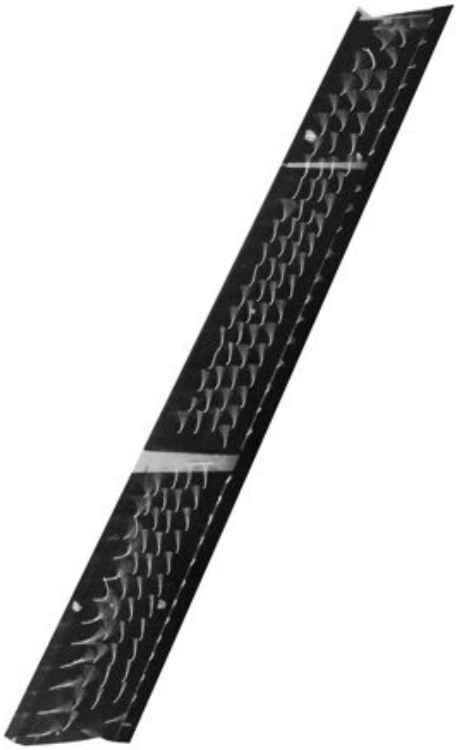

(c) $Ail = 16.0°, M = 0.20$.

(d) $Ail = 25.0°, M = 0.20$.

Fig. 8 Flow visualization of aileron upper surface (AFC-off) for the four aileron deflection angles at $\alpha = 4°$.

C. CRM-HL Takeoff Characteristics, Aileron AFC ON

In this study, increased L/D is achieved by deflecting the aileron beyond the nominal deflection of 7.5° and using AFC to control the flow separation that occurs at higher aileron deflection angles due to the larger adverse pressure gradient. AFC is applied at aileron deflection angles of 16° and 25° in the CFD study of Shmilovich et al. [6]. While L/D could be improved at both aileron deflection angles with AFC, the optimal deflection angle was 16° due to smaller trim drag penalties when compared to the higher deflection angle of 25°. We tested both 16° and 25° aileron deflection angles on the CRM-HL during the 14x22 experiment with $Ail = 16°$ being the primary configuration. The actuator cartridges, located upstream of the aileron leading edge, introduced streamwise vortices into the flowfield to control flow separation. This type of AFC has been successfully demonstrated in numerous experiments with the higher technology readiness level (TRL) flight demonstration of the AFC-enhanced vertical tail [23] being a well-known example. The results presented in the following sections will explore the AFC aileron flowfield as well as the increments in lift and drag due to flow control. The SWJ1 actuator cartridges will be used for this evaluation of aileron flow control. The actuators were tested over an NPR range of 1 to 3. The upper NPR limit of 3 was exceeded for some of the cartridges, especially when the number of actuators was reduced for the SWJ2 and SWJ3 actuator configurations of Table 2. Most of the actuator cartridges were evaluated over an abbreviated angle of attack (0° – 10°) at fixed NPR values to obtain the data needed to assess the L/D benefits of AFC on the drooped aileron. In addition to the α sweeps at a fixed NPR, testing was also performed at a fixed α with NPR varied.

Results acquired with α fixed at 4° and NPR, and thus mass flow, varied are examined to determine the flowfield changes due to AFC. Surface pressure results, from the streamwise row of pressures at $\eta = 82\%$, are presented in Fig. 9(a). The C_p distributions are presented with the x coordinates of the wing components in their stowed positions. The results indicate an increase in suction pressure with increasing NPR (i.e., increasing mass flow rate and momentum coefficient) along the entire upper surface of the model at this η location. On the aileron, flow separation with AFC off ($NPR = 1$) is evident by dCp/dx being nearly zero for $x > 174$ inches. Fully attached flow on the aileron, if the criterion is $C_{p,TE} \approx 0$, occurs when $NPR \approx 2.0$. As NPR increases beyond $NPR = 2.0$, lift continues to increase as noted by the local increase in suction pressure upstream of the aileron on the upper surface at $\eta = 82\%$ (Fig. 9(a)). The sectional lift coefficient (c_L, not shown) computed using the static pressures at $\eta = 82\%$ increases by 0.12, a local increase in lift of 22%. Results for the streamwise C_p distributions on the most outboard wing section ($\eta = 91\%$) look similar (see Fig. 9(b)). Momentum levels of $NPR \approx 2.0$ introduced into the separated flow on the aileron result in $C_{p,TE} \approx 0$. At this location, c_L is increased by 0.13, resulting in a local increase in lift of 39%. Streamwise C_p results illustrate the local changes to the flowfield over the outboard wing section caused by controlling flow separation on the deflected aileron. The seemingly large changes in the local aileron flowfield have a small impact on the total force coefficients on the model, increasing lift by 0.05 and reducing drag by about 12 drag counts. Local increments in lift on the outboard wing section alter the spanload distribution making it more elliptical resulting in lower induced drag.

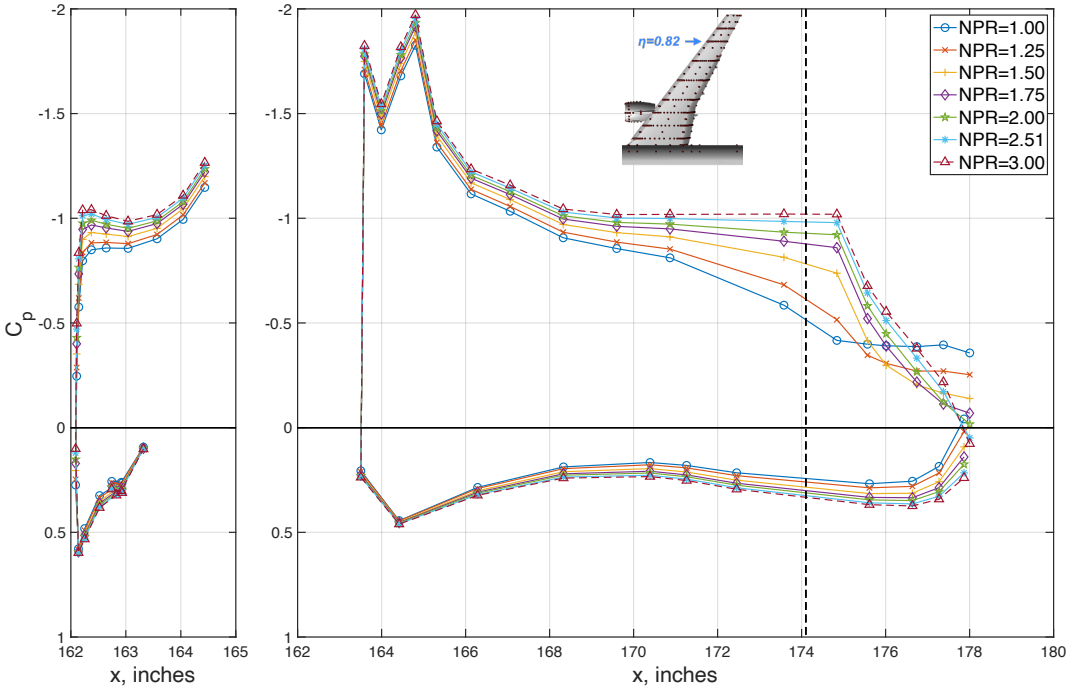

(a) η = **0.82%**.

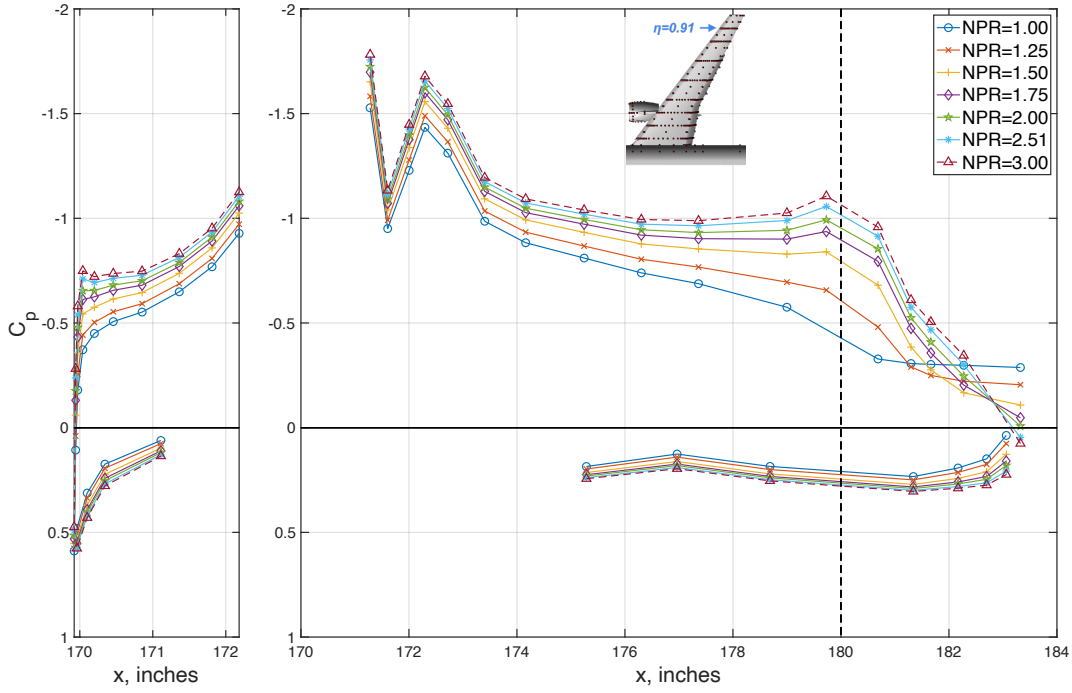

(b) η = **0.91%**.

Fig. 9 C_p Distributions with NPR of SWJ1 varied ($\alpha = 4°$, $Ail = 16°$). Vertical dashed line represents junction between main wing and aileron.

Tuft flow visualization results are presented in Fig. 10 for the NPR levels of 1, 1.5, 2.0, and 3.0 corresponding to the conditions of Fig. 9. With AFC off (Fig. 10(a)), the tuft pattern show that the flow is separated on the entire aileron surface. When SWJ control is applied with $NPR = 1.5$, flow over the upstream portion of the aileron appears to be attached. NPR levels of 2 and above (Fig. 10(c) and 10(d)) cause the tufts to be directed in the streamwise direction,

(a) $NPR = 1$. (b) $NPR = 1.5$. (c) $NPR = 2.0$. (d) $NPR = 3.0$.

Fig. 10 Flow visualization of aileron upper surface (AFC-on) for select NPR values ($Re_c = 3.0x10^6$, $M = 0.2$, $q_\infty = 60$ psf, $\alpha = 4°$).

indicating the flow over most of the aileron surface is attached.

Figure 11(a) presents C_p distributions from the spanwise row of pressures located near the middle of the main element corresponding to the streamwise results presented in Fig. 9. The spanwise row is indicated by the red circles (orifice locations) on the image of the model in the background of the figure. These C_p distributions provide an indication of the spanwise effect of AFC on the aileron. AFC on the aileron increases the suction pressures over the spanwise region (η = 74%–95%) covered by the aileron on the main wing and has a small effect on the local suction pressures inboard of the aileron. The CFD results of Shmilovich et al. [5] also show this effect. Based on the C_p results shown in Fig. 11, the change in suction pressure is consistent with an increase in loading along the span that reduces the induced drag of the wing by providing a more elliptical spanload distribution. Results from static pressure measurements on the model presented thus far show that AFC on the drooped aileron compare well with the trends observed in the CFD predictions [5, 6] used to select this approach for the experimental test campaign.

The main focus of this experiment was to determine the L/D increment that could be obtained on the CRM-HL using pressure and mass flow levels that may be feasible on a commercial transport. We have shown that the spanload distribution of the 10% scale CRM-HL can be altered by applying AFC upstream of a deeper drooped aileron. Figure 12 shows initial results that quantify the improvements in L/D for $Ail = 16°$ with SWJ1 actuators compared to $Ail = 7.5°$. In order to obtain $\Delta L/D$, polynomial curve fits were applied to L/D vs. C_L results at fixed NPR for $Ail = 16°$ using the SWJ1 cartridges. Results from the nominal aileron deflection angle of 7.5° were also fit with the same order polynomial. These functions were then queried for L/D at a given C_L. As previously shown, flow attachment to the aileron occurs at $NPR \approx 2$ based on the C_p distributions of Fig. 9 when using SWJ1 actuators at $Ail = 16°$. The improvement in L/D obtained with $NPR = 2$ is approximately 3.5%. The data used to make these initial estimates have classical wall corrections (blockage and lift interference) applied. These results are more conservative compared to the uncorrected data.

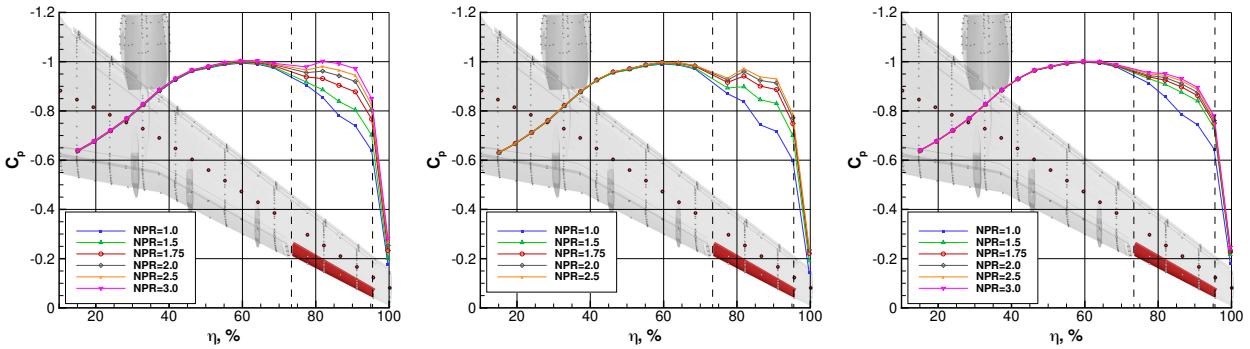

(a) SWJ1. (b) SWJ2. (c) SWJ3.

Fig. 11 Spanwise C_p on main wing of CRM-HL (AFC-on). The aileron surface shaded red, vertical dashed lines indicate aileron extent and red orifices on the wing denote pressure orifices for the presented results (Re_c = 3.0x10^6, M = 0.2, q_∞ = 60 psf, α = 4°, Ail = 16°).

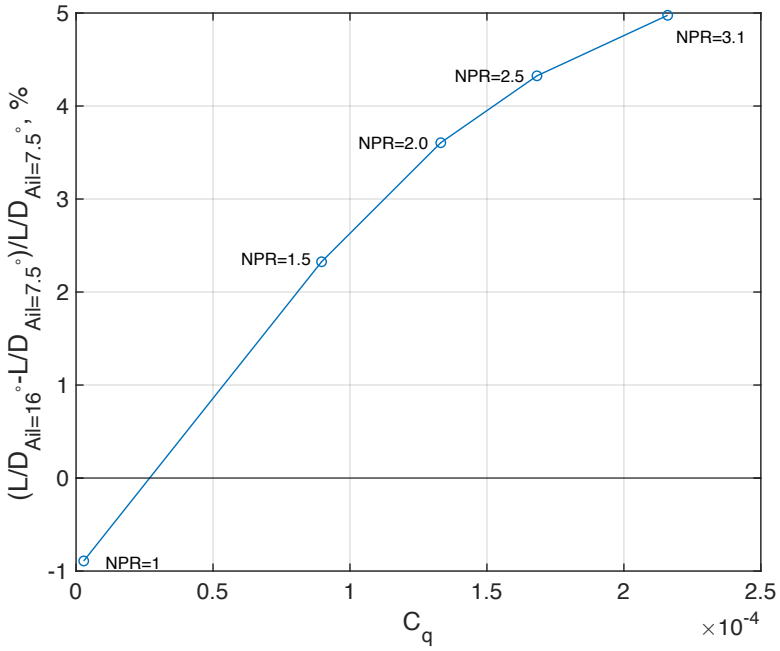

Fig. 12 L/D Increment using SWJ1 (Ail = 16°, Re_c = 3.0x10^6, M = 0.2, q_∞ = 60 psf).

IV. Summary

Drooped aileron active flow control (AFC) was successfully demonstrated to improve the lift to drag ratio (L/D) on the 10% scale, semispan High-Lift Common Research Model (CRM-HL) configured in the takeoff configuration. The takeoff configuration of the CRM-HL model has a leading edge slat deflection angle of 22° and inboard and outboard trailing edge flap deflection angles of 25°. Increments in L/D at takeoff have the potential to increase payload or range and in addition, reduce fuel burn and emissions, if the engine core size can be reduced. These improvements in vehicle efficiency motivated this experimental effort. The AFC aileron application focuses on increasing the aileron deflection beyond the nominal deflection angle of 7.5° and applying AFC to control the separation that occurs at higher deflection angles. This AFC application increases lift locally and reduces the form drag present in the absence of AFC at aileron deflection angles (Ail) of 16° and 25°. Moreover, potential changes to the spanload distribution resulting from increasing lift on the outboard wing section may also reduce the induced drag. Initial results from the recent wind tunnel campaign were presented illustrating the effect on the CRM-HL pressure distributions due to applying AFC on

the aileron. These preliminary results indicate improvements in L/D of approximately 3.5% (at nozzle pressure ratio, $NPR = 2$) when flow separation on the aileron is controlled and the outboard spanload is increased. Data analysis is ongoing and future publications are planned that will include a more detailed analysis of results from the experiment.

Acknowledgments

This research was funded by the Airframe Technologies Subproject of the Advanced Air Transport Technology Project in the NASA Advanced Air Vehicles Program. The authors are extremely grateful to the staff of the 14x22 for their support and the efforts taken to ensure the data quality met the test requirements. The authors also thank model designer Sandy Webb (design of the AFC aileron for the 10% scale model), Danny Lovaglio and Tom Hall (static and dynamic pressure instrumentation), Rob Andrews (SLA actuator fabrication), and the NASA Langley machine shop (pre-test hardware modifications and repairs).

References

[1] Lin, J. C., Melton, L. P., Hannon, J. A., Andino, M. Y., Koklu, M., Paschal, K. B., and Vatsa, V. N., "Semispan Test Results of an Active Flow Control Enabled High-Lift Common Research Model in Landing Configuration," NASA TP 20220015673, December 2022. doi:https://doi.org/2060/20220015673.

[2] Lin, J. C., Melton, L. P., Hannon, J. A., Andino, M. Y., Koklu, M., Paschal, K. B., and Vatsa, V. N., "Testing of High-Lift Common Research Model with Integrated Active Flow Control," *AIAA Journal of Aircraft*, Vol. 57, No. 6, 2020, pp. 1121–1133. doi:https://doi.org/10.2514/1.C035906.

[3] Lin, J. C., Melton, L. P., Hannon, J., Koklu, M., and Andino, M., "Semispan Test Results of a Conventional High-Lift Common Research Model in Landing Configuration," NASA TP 20220008270, August 2022. doi:https://doi.org/2060/20220008270.

[4] Hartwich, P. M., Dickey, E. D., Sclafani, A., Camacho, P., Gonzales, A. B., Lawson, E. L., Mairs, R. Y., and Shmilovich, A., "AFC-Enabled Simplified HIgh-Lift System Integration Study," NASA CR 2014-218521, 2014. doi:https://doi.org/2060/20140012783.

[5] Shmilovich, A., Yadlin, Y., Vijgen, P. M., and Woszidlo, R., "Flow Control for Enhanced Aileron Effectiveness on a Commercial Aircraft," AIAA Paper 2023-0655, January 2023. doi:https://doi.org/10.2514/6.2023-0655.

[6] Shmilovich, A., Stauffer, M., Woszidlo, R., and Vijgen, P., "Low-Speed Performance Enhancement using Localized Active Flow Control: Simulations, Scaling and Design of Localized Active Flow Control on the Common Research Model (4/4)," NASA Contractor or Grantee Report 20220006736, 2022. doi:https://doi.org/2060/20220006736.

[7] Shmilovich, A., Yadlin, Y., Vijgen, P. M., and Woszidlo, R., "Applications of Flow Control to Wing High-Lift Leading Edge Devices on a Commercial Aircraft," AIAA Paper 2023–0656, January 2023. doi:https://doi.org/10.2514/6.2023-0656.

[8] Garner, P., Meredith, P., and Stoner, R., "Areas for Future CFD Development as Illustrated by Transport Aircraft Applications," AIAA Paper 1991–1527, 1991. doi:https://doi.org/10.2514/6.1991-1527.

[9] Vijgen, P. M., Ziebart, A., Shmilovich, A., and Woszidlo, R., "Low-Speed Performance Enhancement using Localized Active Flow Control: Integration Study of Localized Active Flow Control on a Performance Reference Aircraft (3/4)," NASA Contractor or Grantee Report 20220006733, 2022. doi:https://doi.org/2060/20220006733.

[10] Vijgen, P. M., Ziebart, A., Shmilovich, A., and Woszidlo, R., "Conceptual Integration Studies of Localized Active Flow Control on the Wing of a Commercial Aircraft," AIAA Paper 2023–0657, January 2023. doi:https://doi.org/10.2514/6.2023-0657.

[11] Gentry, G. L., Jr., Quinto, P. F., Gatlin, G. M., and Applin, Z. T., "The Langley 14- by 22-Foot Subsonic Tunnel:Description, Flow Characteristics and Guide for Users," NASA TP 3008, 1990. doi:https://doi.org/2060/19900018333.

[12] Neuhart, D. H., and McGinley, C. B., "Free-Stream Turbulence Intensity in the Langley 14- by 22-Foot Subsonic Tunnel," NASA TP 2004-213247, 2004. doi:https://doi.org/2060/20040120956.

[13] Heyson, H. H., "Use of Superposition in Digital Computers to Obtain Wind Tunnel Interference Factors for Arbitrary Configurations, with Particular Reference to V/STOL Models," Tech. Rep. NASA-TR-R-302, 1969.

[14] Vatsa, V. N., Lin, J. C., Melton, L. P., Lockard, D. P., and Ferris, R., "Computational Investigation of Conventional and Active-Flow-Control-Enabled High-Lift Configurations," *AIAA Journal of Aircraft*, Vol. 58, No. 5, 2021, pp. 1137–1153. doi:https://doi.org/10.2514/1.C036233.

[15] Lacy, D. S., and Clark, A. M., "Definition of Initial Landing and Takeoff Reference Configurations for the High Lift Common Research Model (CRM-HL)," AIAA Paper 2020–2771, June 2020. doi:https://doi.org/10.2514/6.2020-2771.

[16] Koklu, M., Lin, J. C., Hannon, J. A., Melton, L. P., Andino, M. Y., Paschal, K. B., and Vatsa, V. N., "Investigation of the Nacelle/Pylon Vortex System on the High-Lift Common Research Model," *AIAA Journal*, Vol. 59, No. 9, 2021, pp. 3748–3763. doi:https://doi.org/10.2514/1.J059869.

[17] 4th AIAA CFD High Lift Prediction Workshop (HLPW-4), January 2022. URL https://hiliftpw.larc.nasa.gov/index-workshop4.html.

[18] Evans, A. N., Lacy, D. S., Smith, I., and Rivers, M. B., "Test Summary of the NASA High-Lift Common Research Model Half-Span at QinetiQ 5-Metre Pressurized Low-Speed Wind Tunnel," AIAA Paper 2020-2770, June 2020. doi: https://doi.org/10.2514/6.2020-2770.

[19] Melton, L. G. P., Lin, J. C., Hannon, J., Koklu, M., Andino, M., and Paschal, K. B., "Sweeping Jet Flow Control on the Simplified High-Lift Version of the Common Research Model," AIAA Paper 2019-3726, June 2019. doi:https://doi.org/10.2514/6.2019-3726.

[20] Koklu, M., "The Effects of Sweeping Jet Actuator Parameters on Flow Separation Control," AIAA Paper 2015–2485, June 2015. doi:https://doi.org/10.2514/6.2015-2485.

[21] Wahls, R., J.B. Adcock, D., and Wright, F., "A Longitudinal Aerodynamic Data Repeatability Study for a Commercial Transport Model Test in the National Transonic Facility," NASA TP 3522, 1995. doi:https://doi.org/2060/19960002985.

[22] Hannon, J. A., Washburn, A. E., Jenkins, L. N., and Watson, R. D., "Trapezoidal Wing Experimental Repeatability and Velocity Profiles in the 14- by 22-Foot Subsonic Tunnel (Invited)," AIAA Paper 2012–0706, January 2012. doi: https://doi.org/10.2514/6.2012-706.

[23] Whalen, E. A., Shmilovich, A., Spoor, M., Tran, J., Vijgen, P., Lin, J. C., and Andino, M. Y., "Flight Test of an Active Flow Control Enhanced Vertical Tail," *AIAA Journal*, Vol. 56, No. 9, 2018, pp. 3393–3398. doi:https://doi.org/10.2514/1.J056959.